

Centrality and $\sqrt{s_{NN}}$ Dependence of the $dE_T/d\eta$ and $dN_{ch}/d\eta$ in Heavy Ion Collisions at Mid-rapidity

A. Milov for the PHENIX Collaboration¹

Department of Physics and Astronomy, Stony Brook University, SUNY, Stony Brook, NY 11794, USA

Abstract. The PHENIX experiment at RHIC has measured transverse energy and charged particle multiplicity at mid-rapidity in $Au + Au$ collisions at $\sqrt{s_{NN}} = 19.6, 130, 62.4$ and 200 GeV as a function of centrality. The presented results are compared to measurements from other RHIC experiments, and experiments at lower energies. The $\sqrt{s_{NN}}$ dependence of $dE_T/d\eta$ and $dN_{ch}/d\eta$ per pair of participants is consistent with logarithmic scaling for the most central events. The centrality dependence of $dE_T/d\eta$ and $dN_{ch}/d\eta$ is similar at all measured incident energies. At RHIC energies the ratio of transverse energy per charged particle was found independent of centrality and growing slowly with $\sqrt{s_{NN}}$. A survey of comparisons between the data and available theoretical models is also presented.

1. Introduction

The PHENIX experiment at the Relativistic Heavy Ion Collider (RHIC) at Brookhaven National Laboratory was designed to measure the properties of matter at extremely high temperatures and densities. Under such conditions, there is possibility to produce states of matter that have yet to be observed or studied in the laboratory. The best known of these is the *quark-gluon plasma* (QGP), a form of matter where quarks are not confined within individual baryons but exist as some form of plasma of individual quarks and gluons. It should be emphasized that the exact properties of this matter are not known and that the characterization of the deconfined state, if such a state is produced, is an essential part of the RHIC program.

One fundamental element of the study of ultrarelativistic collisions is the characterization of the interaction in terms of variables such as the energy produced transverse to the beam direction and the number of charged particles. These two variables are closely related to the collision geometry and are important in understanding global properties of the system during the collision.

This paper describes a systematic study of $dE_T/d\eta$ and $dN_{ch}/d\eta$ at mid-rapidity² by the PHENIX experiment at center-of-mass energies $\sqrt{s_{NN}} = 19.6, 130, 62.4$ and 200 GeV. The centrality dependence of E_T and N_{ch} is characterized by the number of participants, determined with a Glauber model, and is studied as function of the incident energy. E_T and N_{ch} results for all four RHIC measurements are included as part of this study. The data taken at 19.6 GeV is particularly interesting because it allows a close comparison to the lower energies of the CERN SPS program. Comparisons are also made to previous experiments at the Brookhaven AGS and

¹ For the full list of authors and acknowledgments see reference [1]

² Also referred as E_T and N_{ch} in this paper.

CERN SPS at center-of-mass energies of 4.8 GeV, 8.7 GeV, and 17.2 GeV. Finally, an extensive set of collision models describing the E_T and N_{ch} distributions are compared to the existing data.

2. PHENIX detector and Analysis

PHENIX is one of four experiments located at RHIC [2]. The PHENIX detector consists of two central spectrometer arms, designated east and west for their location relative to the interaction region, and two muon spectrometers, similarly called north and south. Each central spectrometer arm covers a rapidity range of $|\eta| < 0.35$ and subtends 90° in azimuth. The muon spectrometers both have full azimuthal coverage with a rapidity ranges of $-2.2 < \eta < -1.2$ (south) and $1.2 < \eta < 2.4$ (north). Additional global detectors are used as inputs to the trigger and for global event characterization such as vertex, time of event and centrality determination. A detailed description of the PHENIX detector can be found in [3].

The PHENIX detector subsystems relevant for the physics analysis published here are: the Pad Chambers used for the charged particle multiplicity measurement, the Electromagnetic Calorimeter used to measure transverse energy, the Beam-Beam Counter and the Zero Degree Calorimeter, the two detectors used for triggering and centrality determination are described in publications [4, 5, 6, 7].

The analysis procedures to measure E_T and N_{ch} are described in details in publications [10, 11, 12, 13]. Some additional information concerning the analysis at $\sqrt{s_{NN}} = 19.6$ GeV can be found in [1]. The preliminary results on $dN_{ch}/d\eta$ at $\sqrt{s_{NN}} = 62.4$ GeV use the same technique as implemented at other energies.

For the sake of space we only mention errors relevant to the analyses. Statistical errors are small and do not exceed 1% of the measured value. The systematic errors are summarized in Table 1. The errors for the lowest and the highest incident energy are listed, whereas at all other energies they are close to these values. The systematic errors for both measured values are of two types. The first type affects the centrality dependence. It is listed in the Table 1 with the range (first number corresponds to the most central bin). Errors of the second type contribute to the overall scaling of the data. In the figures below the centrality dependent errors are shown as a corridor, and the full systematic error is shown with the error bars³. Centrality related errors are common to both measured quantities.

Table 1. Summary of systematic errors given in %. When the range is given, the first number corresponds to the most central bin and the second to the most peripheral bin.

$\sqrt{s_{NN}}$ [GeV]	$dE_T/d\eta$		$dN_{ch}/d\eta$	
	19.6	200	19.6	200
Energy resp.	4.7	3.9		
Bkg. / noise	0.5-3.5	0.2-6	1.0	1.0
Acceptance	2.0	2.0	2.3	2.3
In- & outflow	3.0	3.0	5.7	2.9
Occupancy			1.6-0.3	3.5-0.1
Centrality	2.0	0.5	same	
N_p	2.9-6.7	2.8-15.	same	
Trigger	0.4-8.8	0.3-16.	same	

³ Here and everywhere errors correspond to one standard deviation.

3. Results

3.1. PHENIX results

The distribution of the raw transverse energy, $E_{T_{EMC}}$, into the fiducial aperture of two EMCAL sectors is shown in the left three panels of Fig. 1 for three RHIC energies $\sqrt{s_{NN}} = 19.6, 130$ and 200 GeV. The lower scale corresponds to the fully corrected E_T normalized to one unit of pseudorapidity and full azimuthal acceptance. The lower axis in the plot is not labeled beyond 200 GeV to avoid confusion between the true shape of the $dE_T/d\eta$ distribution and E_T as measured using the limited acceptance of two EMCAL sectors.

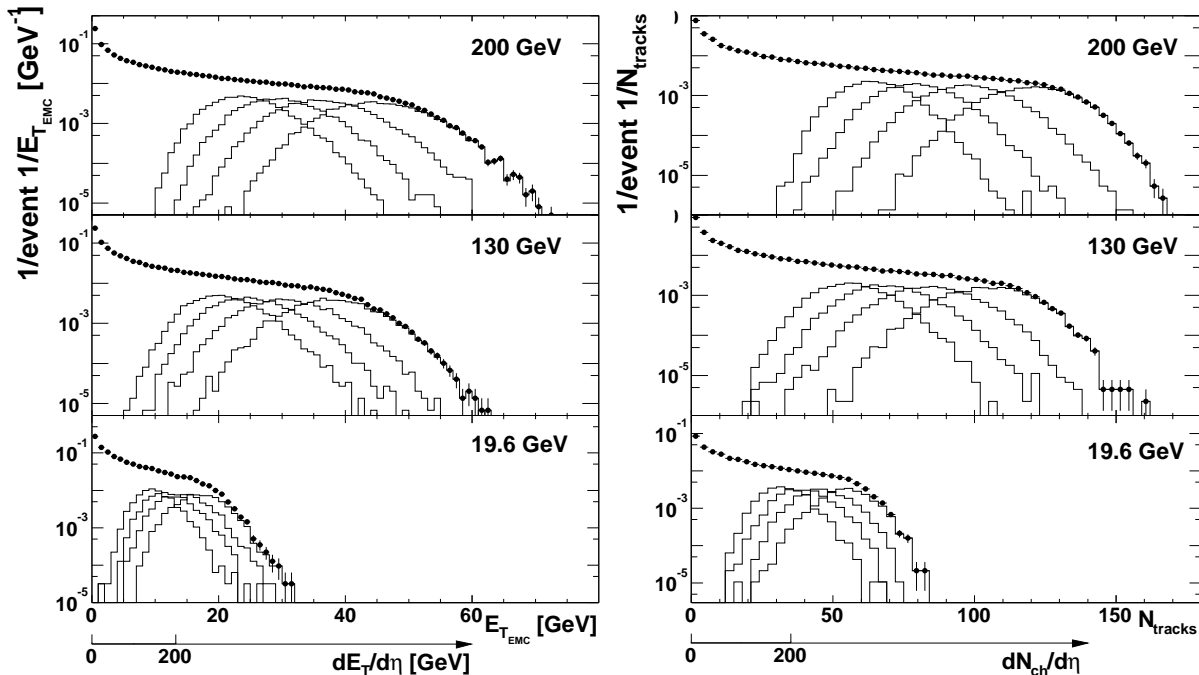


Figure 1. The distribution of the raw E_T in two EMCAL sectors (left) and the number of tracks in the east arm of the PHENIX detector (right) per MB trigger, measured at three energies. The lower axis corresponds to mid-rapidity values of $dE_T/d\eta$ and $dN_{ch}/d\eta$ respectively. Distributions of the four 5% most central bins are also shown in each plot.

Two EMCAL sectors each with azimuthal coverage $\Delta\phi = 27^\circ$ were used to make a measurement at $\sqrt{s_{NN}} = 130$ GeV. At other energies we used five EMCAL sectors. Results obtained with different numbers of sectors at the same energy are consistent within 1.5%.

The right three panels in Fig. 1 show the number of tracks reconstructed in the east arm of the PHENIX detector after the background subtraction and all other corrections. The lower axis corresponds to measured distributions normalized to one unit of pseudorapidity and full azimuthal acceptance. For a similar reason as for the E_T , the lower axis is not labeled above 200 GeV in $dN_{ch}/d\eta$.

For the N_{ch} measurements at $\sqrt{s_{NN}} = 130$ GeV, only the east arm was used, while for the other energies the measurements were made using both PHENIX central arms. The results obtained with two arms at $\sqrt{s_{NN}} = 200, 62.4,$ and 19.6 GeV are consistent with each other within 1.5%.

The distributions shown in Fig. 1 have a characteristic shape with a sharp peak that corresponds to the most peripheral events. Missing events caused by the finite MB trigger efficiency in peripheral events would make this peak even sharper than measured. The plateau in all distributions corresponds to mid-central events and the fall-off to the most central $Au + Au$

events. The shape of the curves in Fig. 1 in the fall-off region is a product of the intrinsic fluctuations of the measured quantities and the limited acceptance of the detector.

The distributions for the four most central bins 0%-5% to 15%-20% are also shown in each panel. The centroids of these distributions are used to calculate the centrality dependence of E_T and N_{ch} ⁴. The statistical uncertainty of the mean values (less than or about 1%) determined by the width of the distributions are small because of the large size of the event samples.

The magnitude of $dE_T/d\eta$ at mid-rapidity divided by the number of participant pairs as a function of N_p is shown in Fig. 2. The right three panels show the same ratio for $dN_{ch}/d\eta$ at three RHIC energies.

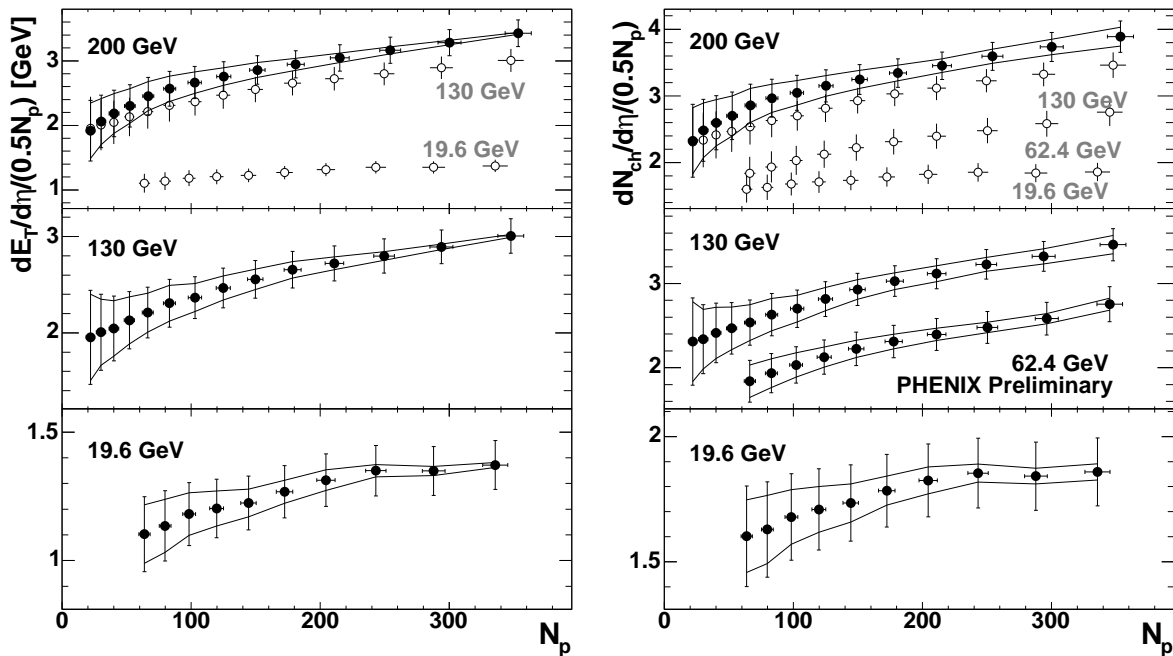


Figure 2. $dE_T/d\eta$ (left) and $dN_{ch}/d\eta$ (right) divided by the number of participant pairs at different RHIC energies. Errors shown with vertical bars are full systematic errors. Lines show the part of the systematic error that allows bending or inclination of the points. Horizontal errors denote the uncertainty in determination of N_p . PHENIX preliminary result for N_{ch} at $\sqrt{s_{NN}} = 62.4$ GeV is shown in the right panel.

The horizontal errors correspond to the uncertainty in N_p , determined within the framework of the Monte Carlo Glauber model. The vertical bars show the full systematic errors of the measurements added quadratically to the errors of N_p . The lines denote the corridor in which the points can be inclined or bent. The statistical errors are smaller than the size of the markers. The upper panel also shows the results of the two lower panels with open markers for comparison.

An important result for Fig. 2 is the consistency evident in the behavior of the centrality curves of E_T shown on the left and N_{ch} shown on the right for all measured energies. Both values demonstrate an increase from peripheral (65%-70%) to the most central events by (50-70)% at RHIC energies $\sqrt{s_{NN}}=130$ GeV and 200 GeV. For the lowest RHIC energy ($\sqrt{s_{NN}}=19.6$ GeV) this increase is at the level of systematic uncertainties of the measurement. One can note that results from PHOBOS [50], show that the total charged particle multiplicity is proportional

⁴ All plotted and quoted numbers correspond to the centrality bin-by-bin average values or ratios of corresponding averages.

to N_p while the multiplicity at mid-rapidity over N_p increases with N_p , indicating that the pseudorapidity distribution gets more narrow for central events. Figure 2 also show the PHENIX preliminary result for N_{ch} at $\sqrt{s_{NN}} = 62.4$ GeV added to the central panel.

The ratios of the $dE_T/d\eta$ and $dN_{ch}/d\eta$ per participant pair measured at different RHIC energies are shown in Fig. 3. In these ratios some common systematic errors cancel.

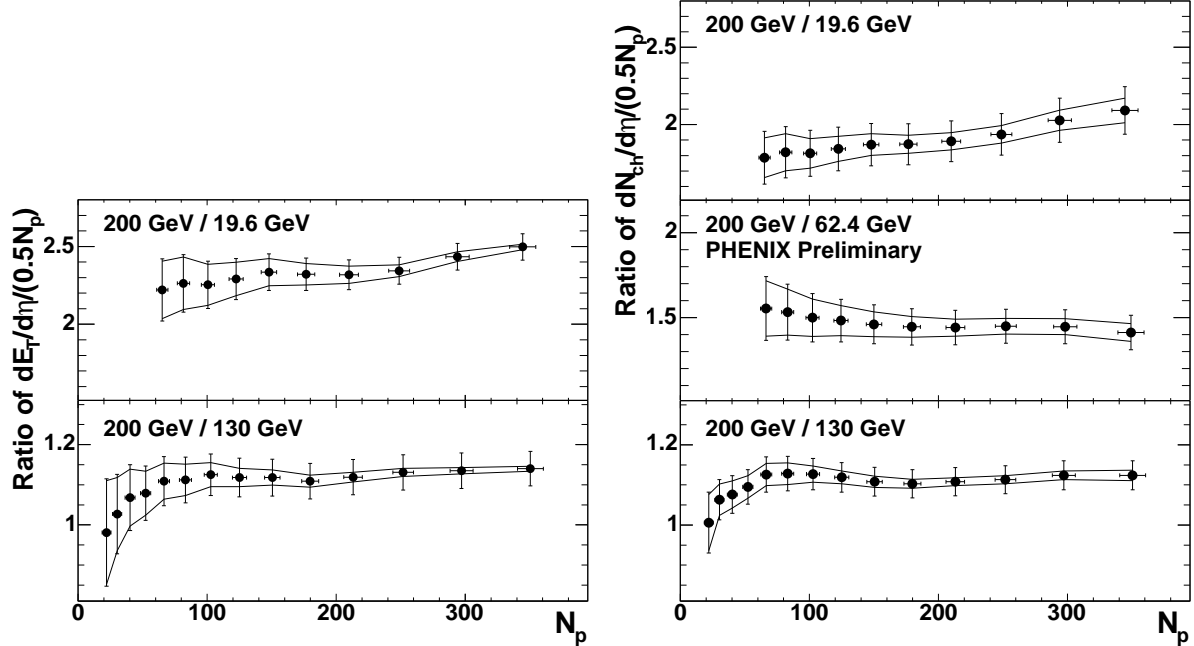


Figure 3. Ratios of $dE_T/d\eta$ (left) and $dN_{ch}/d\eta$ (right) measured at different RHIC energies. The errors shown with vertical bars are the full systematic errors. Lines show that part of the systematic error that allows bending or inclination of the points. The horizontal errors denote the uncertainty in the determination of N_p .

The increase in the E_T production between 19.6 GeV and 200 GeV (with an average factor of 2.3) is larger than for N_{ch} (with average factor of 1.9). This is consistent with an increase in the particle production per participant common to both E_T and N_{ch} and a $\sim 20\%$ increase in $\langle m_T \rangle$ of produced particles contributing to the E_T parameter only.

The ratio of 200 GeV/19.6 GeV shows an increase from peripheral to central events; however the increase is marginal in comparison to the systematic errors of the measurement.

The ratio of 200 GeV/130 GeV is flat above $N_p \sim 80$ and is equal to 1.140 ± 0.043 for E_T and 1.126 ± 0.036 for N_{ch} in the most central bin. A rather sharp increase in the ratios of both quantities between $N_p = 22$ and 83 in the ratios of both quantities is still at the level of systematic uncertainties.

The preliminary ratio of 200 GeV/62.4 GeV although shows the decrease with N_p which is within the systematic errors. The increase in the particle production between these two energies is about 40%.

The ratio of the transverse energy and charged particle multiplicity at mid-rapidity as a function of centrality is shown in Fig. 4 for the three energies. The upper plot also shows the results displayed in the lower panels for comparison.

The ratio E_T/N_{ch} ⁵, sometimes called the ‘‘Global Barometric Observable’’, triggered

⁵ E_T/N_{ch} is used as a shortcut for $\langle dE_T/d\eta \rangle / \langle dN_{ch}/d\eta \rangle$ at $\eta = 0$ in C.M.S..

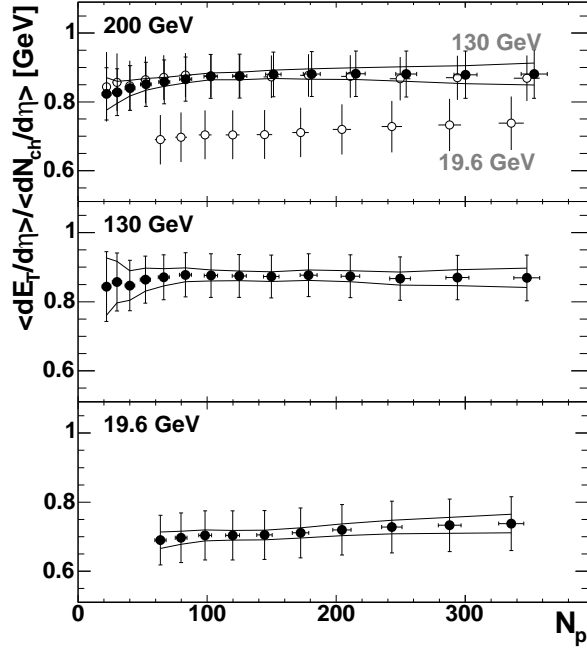


Figure 4. E_T/N_{ch} vs. N_p at different RHIC energies. The errors shown with vertical bars are the full systematic errors. Lines show that part of the systematic error that allows bending or inclination of the points. The horizontal errors denote the uncertainty in the determination of N_p .

considerable discussion [28, 29]. It is related to the $\langle m_T \rangle$ of the produced particles and is observed to be almost independent of centrality and incident energy of the collisions within the systematic errors of the previous measurements. The present paper forges a direct link between the highest SPS and lowest RHIC energies, making a more quantitative study of E_T/N_{ch} possible.

The results presented in Fig. 4 show that the centrality dependence of E_T/N_{ch} is weak and lies within the systematic errors plotted with lines. There is a clear increase in E_T/N_{ch} between $\sqrt{s_{NN}}=19.6$ GeV and 200 GeV. The $\sqrt{s_{NN}}$ dependence of the results is discussed below.

3.2. Bjorken Energy Density

The Bjorken energy density [30] can be obtained using

$$\epsilon_{Bj} = \frac{1}{A_{\perp}\tau} \frac{dE_T}{dy}, \quad (1)$$

where τ is the formation time and A_{\perp} is the nuclei transverse overlap area.

The transverse overlap area of two colliding nuclei was estimated using a Monte Carlo Glauber model $A_{\perp} \sim \sigma_x \sigma_y$, where σ_x and σ_y are the widths of x and y position distributions of the participating nucleons in the transverse plane. The normalization to πR^2 , where R is the sum of r_n and d parameters in a Woods-Saxon parameterization (see e.g.: [1]), was done for the most central collisions at the impact parameter $b = 0$.

For the transformation from $dE_T/d\eta|_{\eta=0}$ to $dE_T/dy|_{y=0}$, a scale factor of 1.25 ± 0.05 was used, see [1] for the details of conversion procedure.

The Bjorken energy density for three RHIC energies is plotted in the left panel of Fig. 5. For the 5% most central collisions, $\epsilon_{Bj} \cdot \tau$ was 2.2 ± 0.2 , 4.7 ± 0.5 and 5.4 ± 0.6 GeV/($fm^2 \cdot c$) for $\sqrt{s_{NN}}=19.6$, 130 and 200 GeV, respectively. These values increase by 2%, 4% and 5%, respectively, for the maximal $N_{part}=394$, as obtained from extrapolation of PHENIX data points. There is a factor of 2.6 increase between the ‘‘SPS’’-like energy ($\sqrt{s_{NN}}=19.6$ GeV) and the top RHIC energy $\sqrt{s_{NN}}=200$ GeV. The comparison of the only published $\epsilon_{Bj}=3.2$ GeV/ fm^3 at SPS [31] and top RHIC energies, assuming the same $\tau=1$ fm/ c , reveals an increase in energy density by

a factor of only 1.8, which may come from an overestimation in the SPS measurement, as shown in the left panel of Fig. 10 below.

Another approach is used by STAR in [38] for the estimate of the transverse overlap area of the two nuclei $A_{\perp} \sim N_p^{2/3}$ in Eq. 1. This approach accounts only for the common area of colliding nucleons, not nuclei. The results differ only in the peripheral bins as shown in the right panel of Fig. 5. For a comparison, the same panel shows the result obtained by STAR which agrees with PHENIX result within systematic errors, displaying a smaller increase of the energy density with N_p .

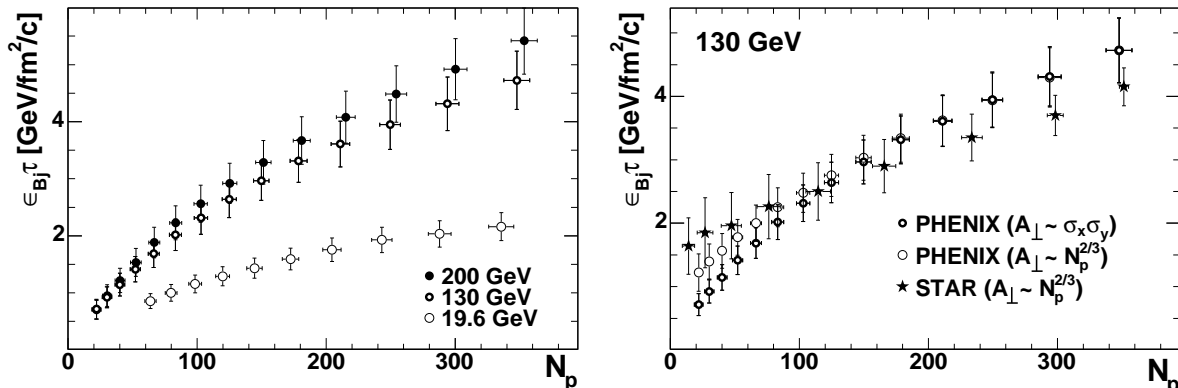


Figure 5. $\epsilon_{Bj} \cdot \tau$ deduced from the PHENIX data at three RHIC energies (left) and using different estimates of the nuclear transverse overlap at $\sqrt{s_{NN}} = 130$ GeV (right).

Can we derive an estimate for τ ? We might say, on general quantum mechanical grounds, that a particle of full energy close to m_T can be considered to have “formed” after a time $t = \hbar/m_T$ since its creation in that frame.

To estimate the average transverse mass, we use the final-state E_T/N_{ch} results presented in Fig. 4. As it was mentioned above, this value is basically independent of centrality and changes from 0.74 GeV to 0.88 GeV for $\sqrt{s_{NN}}$ from 19.6 to 200 GeV. Such estimate would provide us with the formation time τ which is almost the same for all initial conditions of the collisions at RHIC.

An approximate factor of 2/3 is used to account for the total number of particles making the estimate of $\langle m_T \rangle \simeq 0.57$ GeV at $\sqrt{s_{NN}} = 200$ GeV and 130 GeV and $\langle m_T \rangle \simeq 0.50$ GeV at $\sqrt{s_{NN}} = 19.5$ GeV. This results in a formation time of $\tau \simeq 0.35$ fm/c and 0.40 fm/c at these energies respectively. Then for the 5% most central events the estimate of the Bjorken energy at the three RHIC energies are 5.5 GeV/fm³, 13 GeV/fm³ and 15 GeV/fm³.

3.3. Comparison to other measurements

Several factors complicate the comparison between the results of PHENIX and the results of other experiments. AGS and SPS data were taken in the Laboratory (Lab.) system while the RHIC data are in the Center of Mass (C.M.S.) system. Since η and E_T are not boost invariant quantities, the data should be converted into the same coordinate system. Some experiments provide a complete set of identified particle spectra from which information about E_T and N_{ch} can be deduced, while other experiments require additional assumptions to extract $dE_T/d\eta$ and $dN_{ch}/d\eta$ from their results. Publication [1] discusses it in details

The PHENIX results for N_{ch} are compared to the data available from the other RHIC experiments. This comparison is shown in the left panels of Fig. 6.

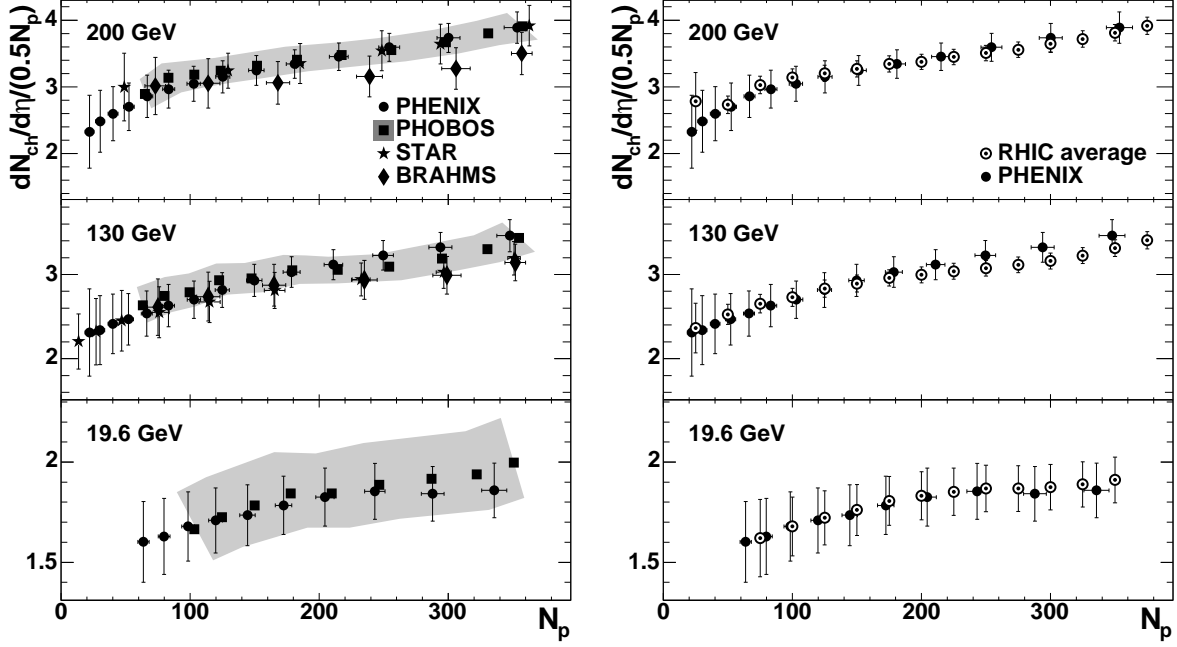


Figure 6. Left panel: $dN_{ch}/d\eta$ per pair of N_p measured by the four RHIC experiments at different energies. The shaded area is the PHOBOS systematic error. Right panel: RHIC average values (including PHENIX) compared to the PHENIX results.

There is good agreement between the results of BRAHMS [39, 40], PHENIX, PHOBOS [41, 42, 43] and STAR [44, 45] using N_p based on a Monte-Carlo Glauber model. This agreement is very impressive because all four experiments use different apparatuses and techniques to measure the charged particle production. The systematic errors of all results are uncorrelated, except for errors due to the same Glauber model which are small. That makes it possible to calculate the RHIC average and reduce the systematic uncertainty. The averaged results from all four RHIC experiments are plotted in the right panel of Fig. 6. The procedure of the calculating the average is the same as used in [21] and is also explained in [1].

Figure 7 compares E_T results from the PHENIX and STAR [46] experiments. The results are consistent for all centralities within systematic errors, though STAR $dE_T/d\eta$ per participant pair as shown in the upper panel has a smaller slope for N_p in going from semi-peripheral to central collisions and E_T/N_{ch} shown in the lower panel is consistent for all N_p .

The RHIC run at $\sqrt{s_{NN}}=19.6$ GeV allows us to make a connection between RHIC and SPS data. The highest SPS energy of 158A GeV corresponds to $\sqrt{s_{NN}} = 17.2$ GeV in the C.M.S., making a direct comparison of RHIC and SPS results possible. This comparison is shown in Fig. 8. The SPS data is taken from [18, 19, 20, 26, 68, 48] details of the data compilation are explained in [1].

Several comments should be made about this comparison. For both measured parameters the PHENIX results and the SPS results agree. The WA98 results are systematically higher, especially for $dE_T/d\eta$. However the WA98 data has an additional systematic error common to all points shown for the last bin. For N_{ch} the relative spread of the SPS results is larger than for the RHIC results shown in Fig. 6, though overall the $\sqrt{s_{NN}}=17.2$ GeV SPS measurements are consistent with the PHENIX result at $\sqrt{s_{NN}} = 19.6$ GeV. The NA57 results at this energy and at lower energy are published without systematic errors [49], so they cannot be compared to other results on the same basis.

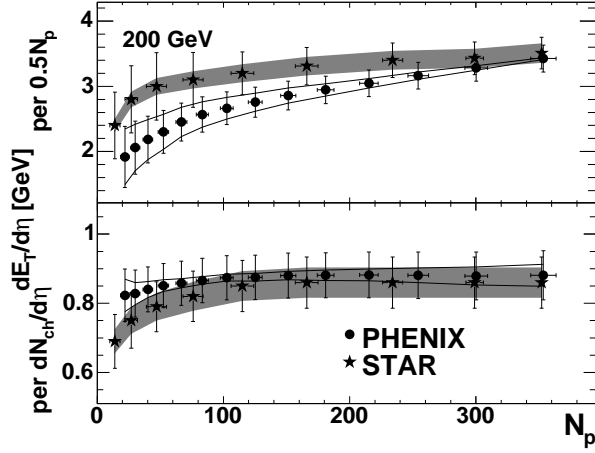


Figure 7. $dE_T/d\eta$ divided by the number of N_p pairs (top) and E_T/N_{ch} (bottom) measured by the PHENIX and STAR [46] experiments at $\sqrt{s_{NN}}=200$ GeV. PHENIX systematic errors are explained in the text. The shaded area is the STAR systematic scaling error.

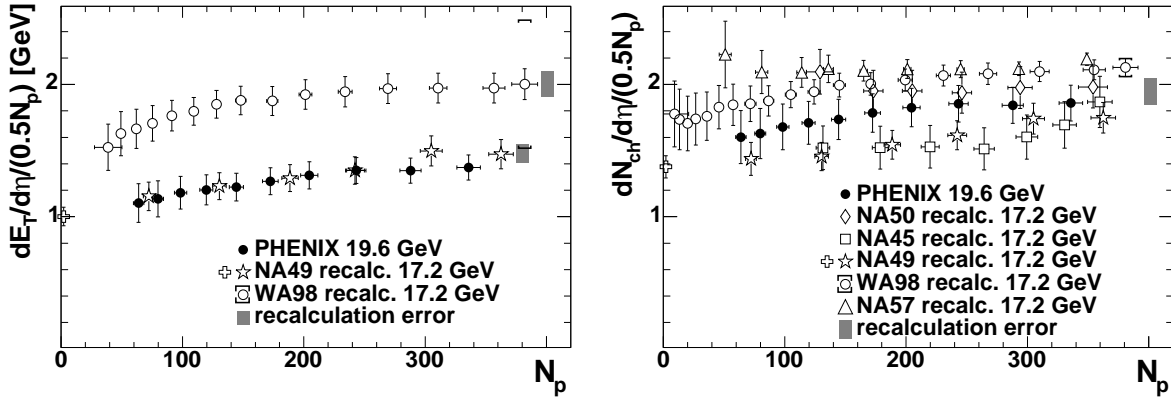


Figure 8. $dE_T/d\eta$ (left) and $dN_{ch}/d\eta$ (right) divided by the number of N_p pairs measured by PHENIX at $\sqrt{s_{NN}}=19.6$ GeV (solid markers) and recalculated from the results of the SPS experiments at the highest energy $\sqrt{s_{NN}}=17.2$ GeV (open markers). The $p + p$ result of NA49 is marked with an open cross.

Different SPS and AGS experiments made measurements at lower energies. The combined data of AGS, SPS and RHIC provide a complete picture of the centrality behavior of E_T and N_{ch} as a function of the nucleon-nucleon energy. The centrality dependence of $dN_{ch}/d\eta$ at mid-rapidity measured at $\sqrt{s_{NN}}=4.8, 8.7$ and 17.2 GeV by different experiments is shown in Fig. 9. The data is taken from [19, 20, 47, 48, 69, 70, 71, 72, 73, 74, 75] and the details of data compilation can be found in [1].

At the highest SPS energy the averaging procedure is the same as for RHIC energies and weighted experimental errors are scaled with the reduced χ^2 -like factor S reaching the value of 1.5 at some points. For the intermediate SPS energy $\sqrt{s_{NN}}=8.7$ GeV, two experiments NA45 [47] and NA50 [48] reported the centrality dependence of $dN_{ch}/d\eta$ at mid-rapidity. The discrepancy in the measurements is approximately three times the quadratic sum of their systematic errors. However the shapes of the two curves are almost the same. NA49 has published results [19, 20] which give one point in $dN_{ch}/d\eta$ at $N_p = 352$. This point favors the NA45 result. The NA57 results [49] also plotted in the Fig. 9 demonstrate even larger discrepancy with the NA50 measurements, but these points lack the systematic errors, as we mentioned before.

The average centrality curve is produced by taking into account the shape of the centrality

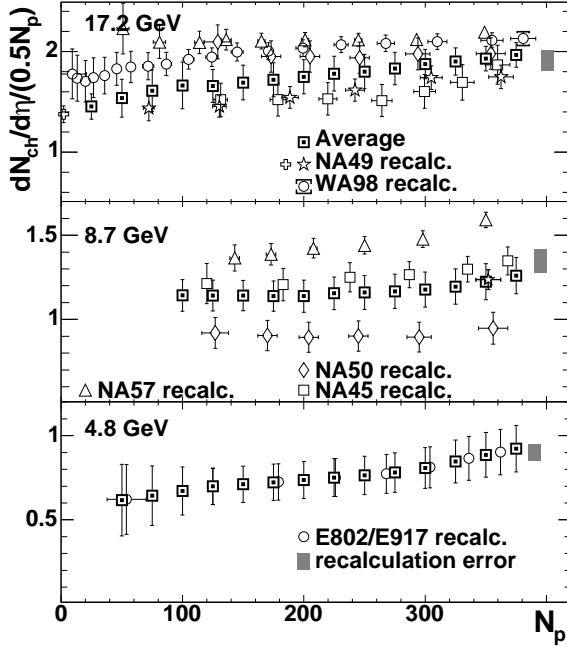


Figure 9. $dN_{ch}/d\eta$ divided by the number of N_p pairs measured by AGS and SPS experiments and the average taken at different energies recalculated in the C.M.S.

curves reported by NA45 and NA50 and the single NA49 point. The errors are scaled with the factor S , which reaches a value of 2.5 at some points. The AGS results are presented with a curve produced from the combined results of the E802/E917 experiments (see publication [1]).

The average SPS centrality dependence at $\sqrt{s_{NN}} = 17.2$ GeV shown in the upper panel in Fig. 9 and the average curve of the two RHIC experiments at $\sqrt{s_{NN}}=19.6$ GeV shown in the lower panel in Fig. 6 are very similar. Less than 5% increase is expected due to the difference in the incident energies between the highest SPS and the lowest RHIC energies (see section 3.4.1 below).

The average values presented in Figs. 6 and 9 are summarized in Table 2.

3.4. Dependence on the incident nucleon energy.

The data compilation made in the previous section allows for a detailed study of the charged particle production in heavy ion reactions at different incident energies of colliding nuclei. Although the data on transverse energy production is not abundant, a similar comparison can be made [10, 11].

3.4.1. Central Collisions Figure 10 shows the energy dependence for the $dE_T/d\eta$ and $dN_{ch}/d\eta$ production per pair of participants in the most central collisions measured by different experiments. See [1] for the details of the data compilation.

The results shown in Fig. 10 are consistent with logarithmic scaling as described in [10, 13, 12]. Use of the logarithmic function is phenomenological and is suggested by the trend of the data in the range of available measurements. The agreement of the fits with the data in both panels is very good, especially in the right panel where the averaged values are used for $N_p = 350$. The single point of NA49 [31] is excluded from the E_T fit. The results of the fit $dX/d\eta = (0.5N_p \cdot A) \ln(\sqrt{s_{NN}}/\sqrt{s_{NN}^0})$ are:

for E_T $\sqrt{s_{NN}^0} = 2.35 \pm 0.2$ GeV and $A = 0.73 \pm 0.03$ GeV

Table 2. Average values of $dN_{ch}/d\eta/(0.5N_p)$ at different $\sqrt{s_{NN}}$. An additional 5% error should be added to columns 17.2 GeV through 4.8 GeV for the uncertainty related to recalculation to the C.M.S..

N_p	200 GeV RHIC aver.	130 GeV RHIC aver.	62.4 GeV PHENIX prelim.	19.6 GeV PHENIX/ PHOBOS	17.2 GeV SPS aver.	8.7 GeV SPS aver.	4.8 GeV E806/E917 combined
375	3.92±0.13	3.41±0.10			1.97±0.12	1.26±0.11	0.92±0.14
350	3.81±0.13	3.31±0.10	2.77±0.21	1.91±0.11	1.93±0.12	1.22±0.11	0.89±0.13
325	3.72±0.12	3.22±0.10	2.68±0.20	1.89±0.11	1.90±0.14	1.20±0.11	0.85±0.13
300	3.65±0.12	3.16±0.10	2.60±0.20	1.88±0.11	1.88±0.15	1.18±0.10	0.81±0.12
275	3.56±0.12	3.11±0.09	2.54±0.19	1.87±0.11	1.83±0.16	1.17±0.10	0.78±0.12
250	3.51±0.12	3.07±0.09	2.48±0.19	1.87±0.12	1.80±0.17	1.16±0.10	0.76±0.11
225	3.45±0.12	3.04±0.10	2.43±0.19	1.85±0.12	1.78±0.17	1.16±0.10	0.75±0.11
200	3.38±0.11	3.00±0.09	2.37±0.19	1.83±0.12	1.75±0.17	1.14±0.10	0.74±0.11
175	3.34±0.12	2.96±0.10	2.30±0.19	1.81±0.12	1.72±0.17	1.14±0.09	0.72±0.11
150	3.27±0.12	2.89±0.10	2.23±0.20	1.76±0.13	1.69±0.17	1.14±0.09	0.71±0.11
125	3.20±0.12	2.83±0.10	2.13±0.20	1.72±0.14	1.66±0.16	1.14±0.09	0.70±0.11
100	3.14±0.13	2.73±0.11	2.02±0.22	1.68±0.15	1.66±0.23	1.14±0.09	0.67±0.14
75	3.03±0.13	2.65±0.11	1.89±0.24	1.62±0.19	1.61±0.21		0.64±0.18
50	2.73±0.13	2.53±0.12			1.54±0.19		0.63±0.21
25	2.78±0.43	2.36±0.30			1.45±0.13		

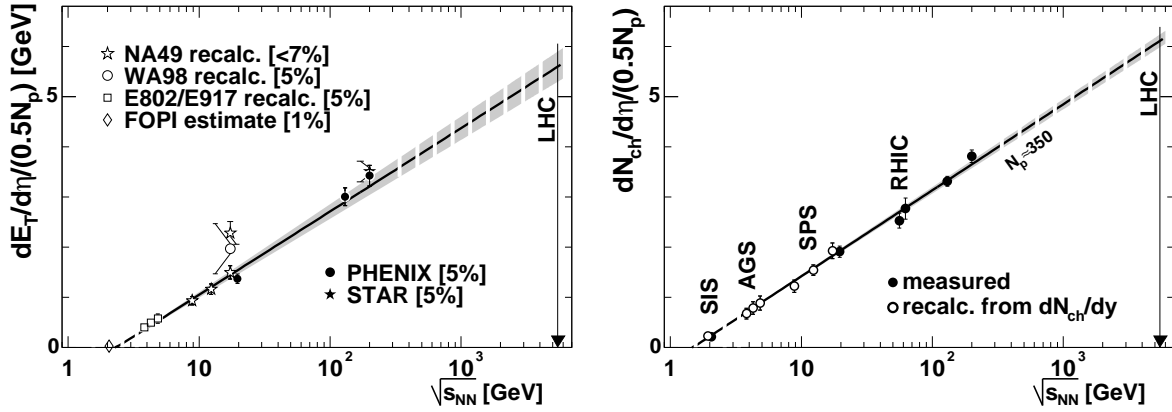


Figure 10. Left panel: $dE_T/d\eta$ divided by the number of N_p pairs measured in the most central bin (value given in brackets) as a function of incident nucleon energy. The line is a logarithmic fit. The band corresponds to a 1σ statistical deviation of the fit parameters. Right panel: the same for $dN_{ch}/d\eta$. The values of N_{ch} are the average values corresponding to $N_p = 350$. The single point at $\sqrt{s_{NN}} = 56$ GeV is based on [41].

for $N_{ch} \sqrt{s_{NN}^0} = 1.48 \pm 0.02$ GeV and $A = 0.74 \pm 0.01$.

The parameter $\sqrt{s_{NN}^0} = 2.35$ GeV obtained from the E_T fit is slightly above, although within 3σ from the minimum possible value of $\sqrt{s_{NN}} = 2 \times a.m.u. = 1.86$ GeV. The measurement closest to it at $\sqrt{s_{NN}} = 2.05$ GeV done by the FOPI experiment allows to estimate the amount of $dE_T/d\eta$ produced to be 5.0 GeV in the most central collisions corresponding to $N_p = 359$. Publication [1]

gives details of the estimate. This does not disagree with the extrapolation of the fit but does indicate that the logarithmic parameterization requires higher order terms to describe how the E_T production starts at very low $\sqrt{s_{NN}}$.

The right panel of Fig. 10 shows the logarithmic fit to the N_{ch} data. It agrees well with all $dN_{ch}/d\eta$ results plotted for $N_p=350$. Unlike that for E_T , the fit parameter $\sqrt{s_{NN}^0}$ for N_{ch} is 1.48 ± 0.02 GeV which is lower than the minimum allowed $\sqrt{s_{NN}}$. This suggests that above $2 \times a.m.u.$ the N_{ch} production as a function of $\sqrt{s_{NN}}$ should undergo threshold-like behavior, unlike the E_T production which must approach zero smoothly due to energy conservation.

The FOPI measurement at $\sqrt{s_{NN}}=1.94$ GeV and 2.05 GeV agrees with the extrapolation of the fit at energy very close to $2 \times a.m.u.$. It is an interesting result that colliding nuclei with kinetic energies of 0.037 GeV and 0.095 GeV per nucleon in the C.M.S. follow the same particle production trend as seen at AGS, SPS and RHIC energies.

A fit to the charged particle multiplicity shows a factor of 2.2 increase in $dN_{ch}/d\eta$ per participant in the most central events from the highest energy at the AGS ($\sqrt{s_{NN}}=4.8$ GeV) to the highest energy at the SPS ($\sqrt{s_{NN}}=17.2$ GeV) and a factor of 2.0 from the highest SPS energy to the highest RHIC energy ($\sqrt{s_{NN}}=200$ GeV). Assuming the same behavior extends to the LHC highest energy $\sqrt{s_{NN}}=5500$ GeV one would expect $dN_{ch}/d\eta = (6.1 \pm 0.13) \cdot (0.5N_p)$ and the increase in particle production from the highest RHIC energy to be $\sim 60\%$ for the most central events. With the greater energy, the rapidity width should increase by $\sim 60\%$ i.e. the total charged particle multiplicity would increase by a factor of ~ 2.6 from the top RHIC energy.

It is interesting to compare the $\sqrt{s_{NN}}$ dependence shown in Fig. 10 to the similar plot for dN_{ch}/dy vs. $\sqrt{s_{NN}}$ published in [32]. In Fig.4 of that publication the energy dependence of dN_{ch}/dy for $N_p=350$ changes the slope between AGS and lower SPS energy. That is not seen in Fig. 10. The parameterization suggested in publication [32], $dN_{ch}/dy \propto (\sqrt{s_{NN}})^{0.3}$ is also different from the logarithmic scaling in Fig. 10. Although quantities in these two figures are not identical, some contribution to the shape of the curve in Fig.4 in [32] may be due to use of logarithmic scale on Y-axis, producing a bend-like shape out of straight line in a linear scale.

The ratio of E_T/N_{ch} for the most central bin as a function of $\sqrt{s_{NN}}$ is shown in Fig. 11. Note

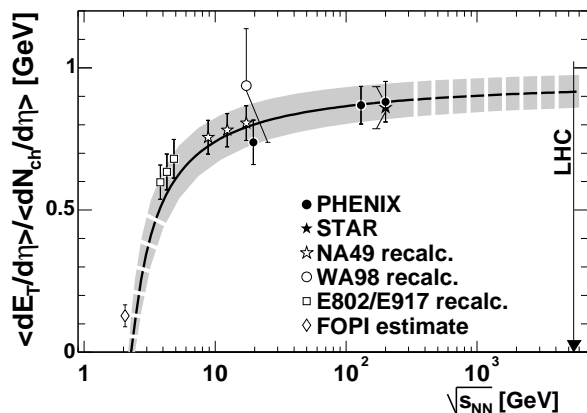


Figure 11. Ratio of E_T over N_{ch} for the most central events as a function of $\sqrt{s_{NN}}$ recalculated into C.M.S.. The line is the ratio of two fits shown in Fig. 10. The band corresponds to one standard deviation of the combined error.

that the line shown in the figure is not the fit to the data points. Rather, it is calculated as a ratio of the fits plotted in Fig. 10. The calculation agrees well with the data.

There are two regions in the plot which can be clearly separated. The region from the lowest allowed $\sqrt{s_{NN}}$ to SPS energy is characterized by a steep increase of the E_T/N_{ch} ratio with $\sqrt{s_{NN}}$. In this region the increase in the incident energy causes an increase in the $\langle m_T \rangle$ of the produced particles. The second region starts at the SPS energies. In this region, the E_T/N_{ch} ratio is very weakly dependent on $\sqrt{s_{NN}}$. The incident energy is converted into particle production at mid-rapidity rather than into increasing the particle $\langle m_T \rangle$.

The shape of the E_T/N_{ch} curve in the first region is governed by the difference in the $\sqrt{s_{NN}^0}$ parameter between E_T and N_{ch} . The second region is dominated by the ratio of the A parameters in the fits; this ratio is close to 1 GeV. Extrapolating to LHC energies one gets a E_T/N_{ch} value of (0.92 ± 0.06) GeV.

The E_T/N_{ch} parameter is usually associated with the chemical freeze-out temperature T . A simple relation like $2/3 E_T/N_{ch} \approx m_0 + 3/2 T$ finds $T \approx 0.22$ GeV for a measured value E_T/N_{ch} of 0.88 GeV at top energy at RHIC. Coefficient 2/3 takes into account neutral particle contribution and the average particle mass $m_0 \approx 0.25$ GeV can be estimated from [17]. The freeze-out temperature estimate of $T \approx 0.22$ GeV extracted this way is in an agreement to $T \approx 0.17$ GeV measured from the spectra [17] plus some contribution of particle flow. In publications [33, 34] authors suggest the same E_T/N_{ch} value close to 1 GeV is valid even at AGS and SIS energies. This is not in disagreement with the curve in Fig. 11 because the E_T definition used in [33, 34], includes full baryon rest mass. We use different definition of E_T as explained in [1] where mass of pre-existing baryons is not included. At lower energy where such contribution to the E_T is larger than at RHIC it would bring the E_T/N_{ch} ratio closer to one.

The transition between two region with different E_T/N_{ch} behavior occurs in the lower SPS energies. There are other observables which also undergo transition between regimes in the same range of $\sqrt{s_{NN}}$. For example, the $\langle K^+ \rangle / \langle \pi^+ \rangle$ ratio demonstrates a peak at around $\sqrt{s_{NN}} \approx 8$ GeV as shown in Fig.4 in reference [35]. In the same region, the volume of the colliding system goes through a minimum as shown in Fig.1 in reference [36]. The asymmetric flow parameter v_2 lies in-plane at and above the highest SPS energy and out-of-plane below it, see Fig.8 in publication [37]. These evidences suggest that the energy range of 5–10 GeV has interesting physics potential which needs to be studied.

3.4.2. Centrality shape Another interesting question is how the shapes of the centrality curves of E_T and N_{ch} change with $\sqrt{s_{NN}}$.

One approach, previously used in a number of papers is to describe the shape of the centrality dependence as a sum of “soft” and “hard” contributions such that the “soft” component is proportional to N_p and the “hard” component to the the number of binary collisions N_c : $A \times N_p + B \times N_c$. A disadvantage of this approach is that the contributions called “soft” and “hard” do not necessarily correspond to the physical processes associated with these notations. Another approach is to assume that the production of E_T and N_{ch} is proportional to N_p^α ; although the parameter α does not have any physical meaning.

We present the results of B/A and α obtained from the fits to the data at different $\sqrt{s_{NN}}$ in Table 3. Although the numbers tend to increase with beam energy, the values presented are consistent with each other within the systematic errors.

Higher quality data would make it possible to derive a more conclusive statement about the shape of the curves plotted in Figs. 6 and 9. With the present set of data, usually limited to N_p above 50, a large part of the centrality curve is missing or smeared by systematic errors. To avoid this, we compare $Au + Au$ collisions to $p + p$ ($N_p=2$) at the same energy.

Figure 12 shows $dN_{ch}/d\eta/(0.5N_p)$ divided by the parameterization plotted in the right panel of Fig. 10. The top panel shows the most central events with $N_p \approx 350$. All points are consistent with one demonstrating an agreement of the fit to the data. The points are connected with a line for visibility. The middle panel shows results for mid-central events with $N_p = 100$ connected with a solid line. The dashed line is the line from the top panel for $N_p = 350$. The points for $N_p = 100$ are lower than $N_p = 350$ by a factor of 0.8 – 0.9, over the plotted range of incident energies. The lower panel shows $p + p$ data corresponding to $N_p = 2$ measured by several experiments. Dashed lines are the same as appear in the upper two panels for $N_p = 350$ and 100

Table 3. “B/A” ratio and parameter α from the fit to the data. Errors are calculated assuming a change of the slope of centrality curves within the limits of the “tilt” errors for PHENIX and full errors for the averaged data (Table 2).

$\sqrt{s_{NN}}$ GeV	$dE_T/d\eta$ PHENIX	$dN_{ch}/d\eta$ PHENIX	$dN_{ch}/d\eta$ Average
B/A			
200	$0.49^{+.69}_{-.22}$	$0.41^{+.57}_{-.21}$	$0.28^{+.18}_{-.15}$
130	$0.41^{+.52}_{-.23}$	$0.41^{+.45}_{-.23}$	$0.26^{+.18}_{-.11}$
19.6	$0.37^{+.48}_{-.22}$	$0.21^{+.30}_{-.15}$	$0.23^{+.73}_{-.23}$
17.2			$0.31^{+.46}_{-.24}$
8.7			$0.12^{+.64}_{-.20}$
parameter α			
200	1.20 ± 0.07	1.18 ± 0.08	1.16 ± 0.06
130	1.14 ± 0.08	1.17 ± 0.08	1.14 ± 0.05
19.6	1.13 ± 0.07	1.09 ± 0.06	1.10 ± 0.11
17.2			1.11 ± 0.08
8.7			1.06 ± 0.13
4.8			1.20 ± 0.24

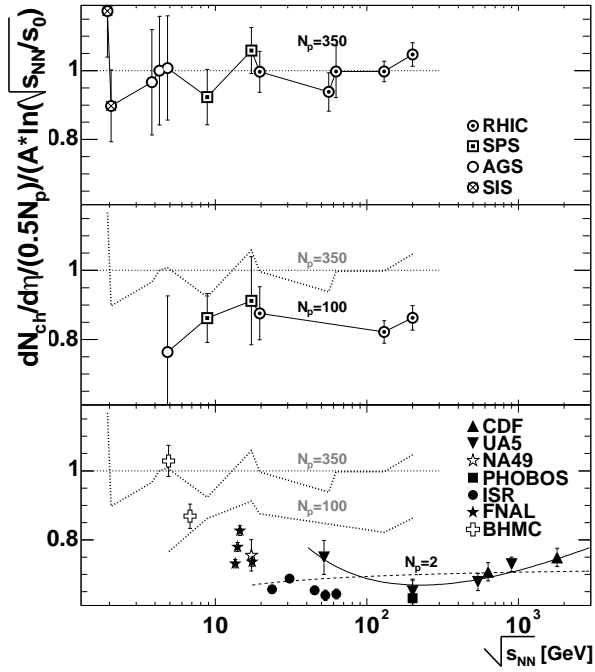


Figure 12. The three panels show $dN_{ch}/d\eta/(.5N_p)$ divided by the logarithmic parameterization from Fig. 10. The panels correspond to $N_p = 350, 100$ and 2 ($p+p$) from top to bottom. $Au + Au$ points are connected with lines also shown in lower panels for comparison. The $Au + Au$ data is tabulated in Table 2; $p + p$ data and parameterizations $dN/d\eta = 2.5 - 0.25\ln(s_{NN}) + 0.023\ln(s_{NN})^2$ (solid line) and $dN/d\eta = 0.27\ln(s_{NN}) - 0.32$ (dashed line) are taken from [51, 52].

and the $p + p$ parameterizations from [51, 52]. In the range of RHIC energies these points are lower by a factor of $0.65 - 0.75$ than the most central. Dotted lines show data from the upper two panels.

These results indicate that the centrality curves normalized to the most central collisions have a similar shape for all RHIC energies within the errors of available measurements.

At lower energies the $p + p$ data show rise and become equal to the most central results. That would mean that at the lower SPS and AGS energies the centrality profile is independent of N_p .

At the same time the cross over takes place at AGS energy and it would suggest that below it the particle production per participant decreases with N_p . There is no measurement supporting such a statement. Also, the the information about $p + p$ particle production at low energies is recalculated from total number of produced particles or identified particles sets which require additional assumptions and systematic uncertainties to be assigned to them. Hence, it is not as reliable as at higher energies.

The data for of the FNAL and BHC collaborations are shown in Fig. 12 as an indication of the trend.

3.5. Comparison to models

A variety of models attempting to describe the behavior of E_T and N_{ch} as a function of centrality at different $\sqrt{s_{NN}}$ are available. An updated set of model results were collected from several theoretical groups to make a comparison as comprehensive as possible⁶.

Figures 13 through 15 show the comparison between the existing theoretical models⁷ and the data for 19.6, 130 and 200 GeV. Brief descriptions of the models and their main characteristics are given below.

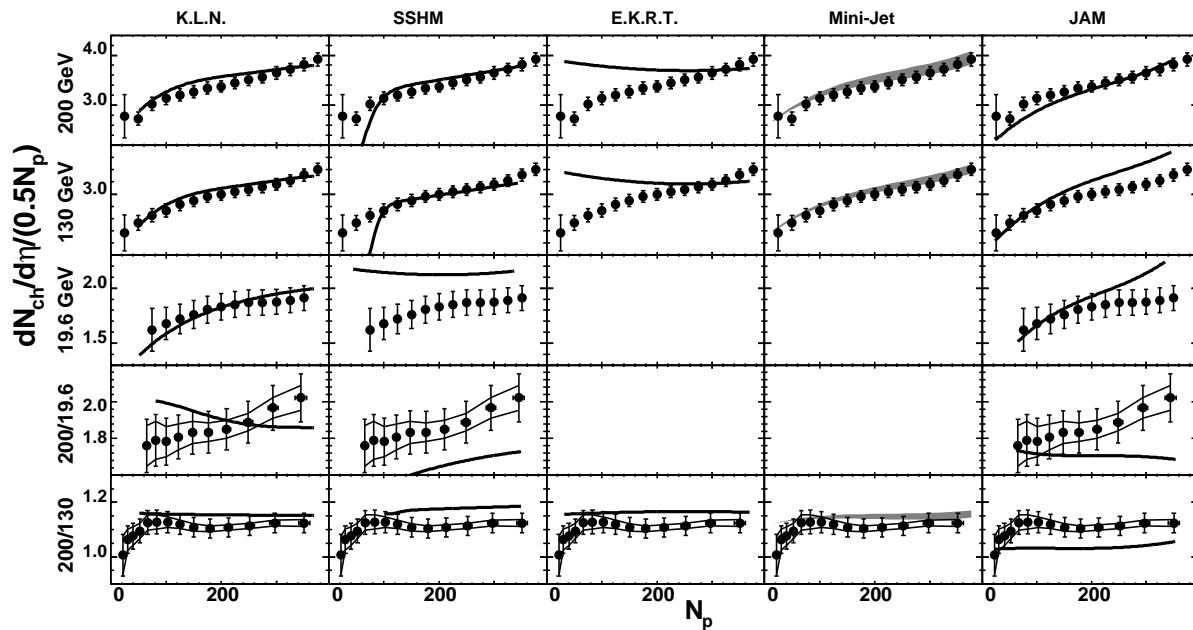


Figure 13. $dN_{ch}/d\eta$ per pair of participants compared to theoretical models. *KLN* [58], *SSHM* [62], *EKRT* [57], *Minijet* [59] and *JAM* [60]. The band shows the range of prediction for the Minijet model.

One of the more commonly used Monte Carlo event generators is *HIJING* [16, 55]. This model, like several others, uses pQCD for initial minijet production, and the Lund string model [56] for jet fragmentation and hadronization. *HIJING* also includes jet quenching and nuclear shadowing. This type of model typically has two components, a soft part proportional to N_p and a hard part proportional to N_{coll} , which partly motivated the discussion in section 3.4.2.

⁶ For the JAM generator authors extracted data by running the code and assigning N_p from the Glauber model simulations.

⁷ Models are presented as the best fit by the polynomial of the lowest degree which is closer than 1% to any theoretical point. The polynomial is plotted in the range where points are provided.

There are also so-called saturation models which also rely on pQCD and predict that at some fixed scale the gluon and quark phase-space density saturates, thus limiting the number of produced quarks and gluons. An example of this type of model is *EKRT* [57], which is referred to as a final state saturation model. In this paper, comparisons are also made to another parton saturation type model, *KLN* [58], an initial state saturation model, and also to models related to *HIJING*, namely *Minijet* [59] and *AMPT* [61]. *AMPT* is a multiphase transport model, and extends *HIJING* by including explicit interactions between initial minijet partons and also final state hadronic interactions. *Minijet* follows the same two-component model as *HIJING* but also incorporates an energy dependent cut-off scale, similar to the saturation models. *JAM* [60] uses *RQMD* and *UrQMD* inspired ideas for the low energy interactions and above resonance region soft string excitation is implemented along the lines of *HIJING*.

The other models are listed briefly below. *SSHM* and *SFM* did not have a designated short identifier, so they were named somewhat arbitrarily here, based on the physics the models incorporate. *SSHM* (*Saturation for Semi-Hard Minijet*) [62] is also a two-component model: pQCD-based for semi-hard partonic interactions, while for the soft particle production it uses the wounded nucleon model. *DSM* [63], the Dual String Model, is basically the Dual Parton Model [64], with the inclusion of strings. *SFM* (*String Fusion Model*) [65], is a string model which includes hard collisions, collectivity in the initial state (string fusion), and rescattering of the produced secondaries. Finally, there are the hadronic models, *LUCIFER* [66], a cascade model, with input fixed from lower energy data, and *LEXUS* [67], a Linear EXtrapolation of Ultrarelativistic nucleon-nucleon Scattering data to nucleus-nucleus collisions.

The available model results range from predicting (or postdicting) $dN_{ch}/d\eta$ at one energy to predicting both $dN_{ch}/d\eta$ and $dE_T/d\eta$ at 19.6, 130 and 200 GeV. The models have varying success in reproducing the data.

Figure 13 shows that *KLN* model is one of the most successful at describing the $dN_{ch}/d\eta$ centrality dependence for all three energies. However, at $\sqrt{s_{NN}}=19.6$ GeV the theoretical curve is steeper than the data. This results in a reversed centrality dependence relative to the data for the 200 GeV to 19.6 GeV ratio. *SSHM* describes the 130 and 200 GeV data well for centralities above $N_p \sim 100$, which is the approximate limit of applicability for this and other saturation models. For the less central events, the models are lower than the data. At 19.6 GeV, the model values are significantly higher than the data. The saturation model *EKRT* describes the central points at both energies but overshoots the more peripheral data points and thus does not reproduce the general centrality dependence of the data. For the non-saturation models included in this figure, *Minijet* reproduces both the overall scale, as well as the centrality and energy dependence of the data rather well.

The *JAM* model shown in Fig. 13 and most of the models included in Fig. 14, provided values for all three energies: 19.6, 130 and 200 GeV. *JAM* is rather successful in describing centrality shape at $\sqrt{s_{NN}}=200$ GeV. It also consistent with the measurements at 130 GeV and partially at 19.6 GeV. In ratios it underestimates the data. For the E_T results shown in Fig. 15 *JAM* reproduced the centrality shapes well, but underestimates the $\sqrt{s_{NN}}$ dependence of the data. *SFM* is in reasonable agreement with the 130 and 200 GeV data, but gives much larger values than the data at 19.6 GeV. *AMPT* is overall in good agreement with the data for the two higher energies, except for the increasing trend in $dN_{ch}/d\eta$ at the most peripheral events, which is not seen in the data. At the lower energy the N_{ch} centrality behavior is underestimated. *LEXUS* severely overshoots the data for all energies, indicating that nucleus-nucleus effects are not correctly accounted for. *LUCIFER* describes the central points at 130 GeV well, but undershoots the less central values at this energy. The *HIJING* models (version 1.37 and a new version with implemented baryon junctions, *HIJING B-B*) only provide points at 130 and 200 GeV and are in reasonable agreement with the data at those energies, but generally give somewhat lower values. The curves shown include quenching and shadowing *HIJING*. *DSM*

describes 19.6 GeV reasonably well for all centralities, and the more central bins for 130 and 200 GeV, but overpredicts the values for semi-central and peripheral events.

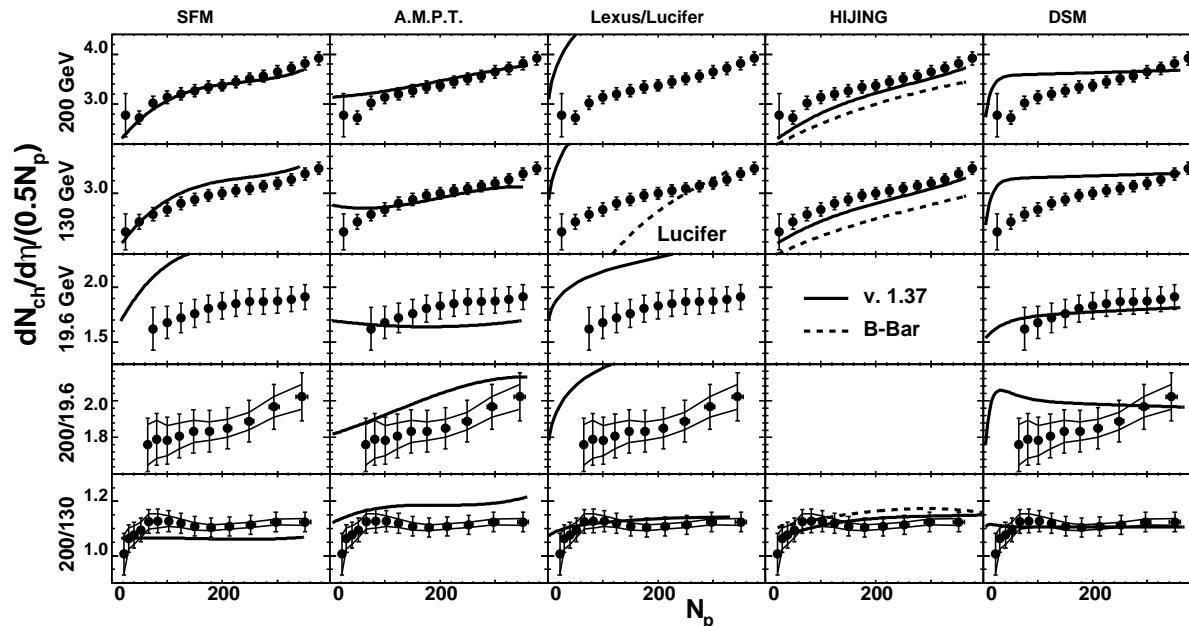


Figure 14. Theoretical models compared to $dN_{ch}/d\eta$ per pair of participants. *SFM* [65], *AMPT* [61], *LEXUS* [67], *LUCIFER* [66], *HIJING* [16, 55] and *DSM* [63].

Figure 15 shows the results for the models that provide data for both $dN_{ch}/d\eta$ and $dE_T/d\eta$. For $dE_T/d\eta$, *LEXUS* and *SFM* consistently overshoot the data for all energies. In the ratio E_T/N_{ch} , *LEXUS* gives values that are too low except at the lowest energy 19.6 GeV. That indicates that the hadronization mechanism allows too little energy per particle. The *SFM* gives values that are too large, except for the most peripheral bin, this suggests, that the particles are assigned transverse masses that are too large. The *HIJING* versions and the related *AMPT* model are in reasonable agreement with the data for both $dE_T/d\eta$ and E_T/N_{ch} ⁸.

Also shown in Fig. 15 are the ratios of results at 200 GeV to 19.6 GeV, and 200 GeV to 130 GeV, for $dE_T/d\eta$. These results, especially the comparison of the 200 GeV to 19.6 GeV data, is intended to make a more precise check of the $\sqrt{s_{NN}}$ dependence of the models. *SFM* fails to describe the 19.6 GeV data and thus can not describe the energy dependence probed by these ratios, unlike *LEXUS* which however does not agree well with the individual data curves for 19.6, 130 and 200 GeV. *AMPT* and the *HIJING* versions reproduce the values of the ratios well, as expected since they are in reasonable agreement with the individual curves. *AMPT* and *HIJING* are also successful in describing the E_T/N_{ch} ratio, as illustrated in the lower panels of Fig. 15.

To summarize, most models reproduce at least some of the data fairly well, but most also fail in describing all the data. Since the model results typically are given without systematic errors, it is not entirely straightforward to quantify the level of agreement or disagreement with the data. Qualitatively, the models that are most successful in describing both $dE_T/d\eta$ and $dN_{ch}/d\eta$ in terms of the overall trends, both regarding centrality dependence and energy dependence, are *AMPT*, and the *HIJING* versions. *KLN* and *Minijet* unfortunately do not give information on

⁸ Note that the *HIJING* versions available at the time the data were collected and used for predictions were in worse agreement with the data [11]. This was before energy loss and minijet separation/cut-off scale parameters were updated.

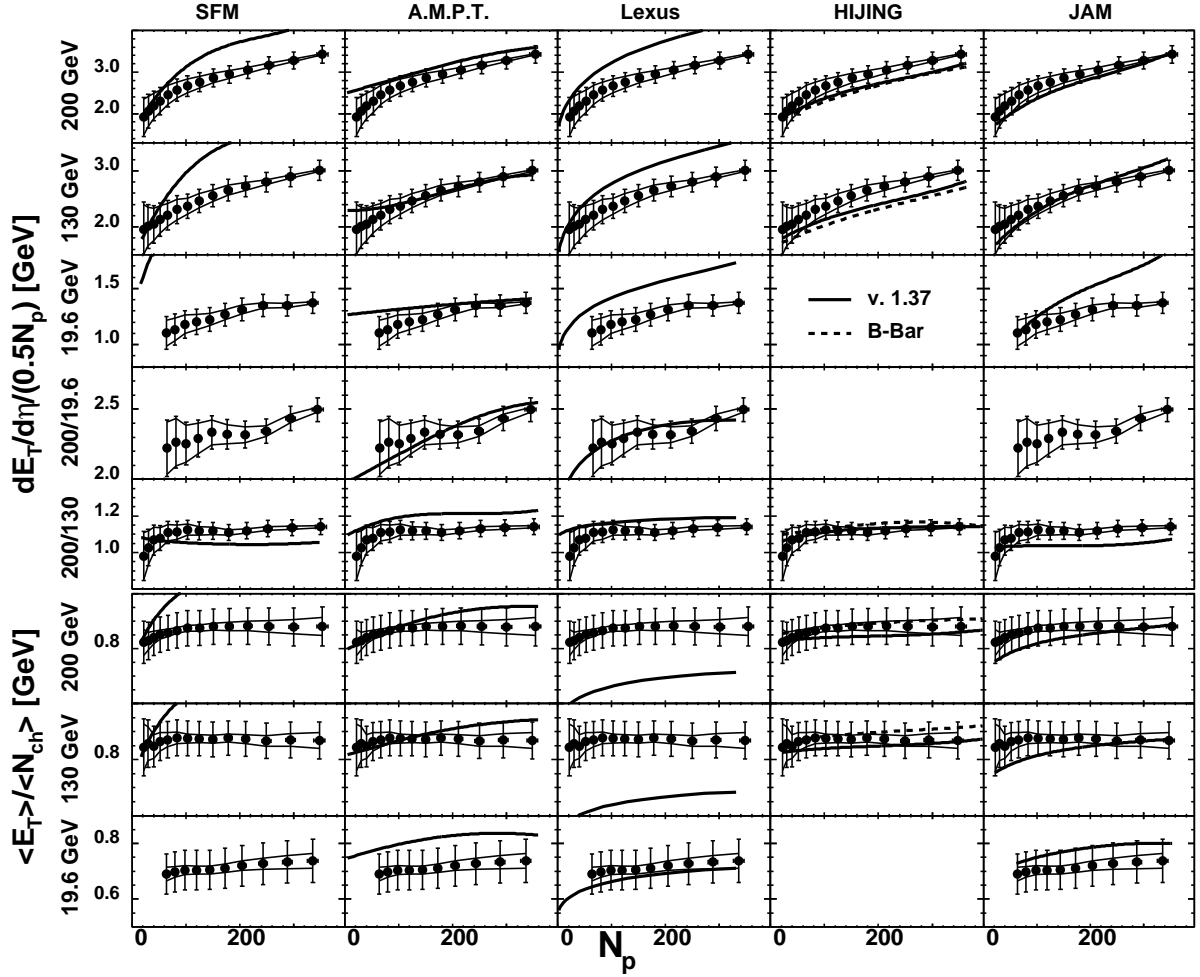


Figure 15. Theoretical models compared to $dE_T/d\eta$ per pair of participants (upper panels) and per produced charged particle (lower panels). *SFM* [65], *AMPT* [61], *LEXUS* [67] and *HIJING* [16, 55].

$dE_T/d\eta$ but are successful in describing the $dN_{ch}/d\eta$ results. The $dN_{ch}/d\eta$ results thus can either be described by the initial state saturation scenario (*KLN*) or by the mini-jet models that need an energy-dependent mini-jet cut-off scale as described in [55, 59] to reproduce the data.

4. Summary

This paper presents a systematic study of the energy and centrality dependence of the charged particle multiplicity and transverse energy at mid-rapidity at $\sqrt{s_{NN}} = 19.6, 130$ and 200 GeV.

The yields, divided by the number of participant nucleons, show a consistent centrality dependence (increase from peripheral to central) between $dE_T/d\eta$ and $dN_{ch}/d\eta$ for all energies. Furthermore, the increase in the ratio E_T/N_{ch} from 19.6 GeV to 200 GeV is consistent with a 20% increase in $\langle m_T \rangle$ with increasing $\sqrt{s_{NN}}$. The ratio E_T/N_{ch} shows only a weak centrality dependence at RHIC energies.

For the $\sqrt{s_{NN}}$ dependence, comparisons were made not only among RHIC results but also including data from lower energy fixed-target experiments at SPS, AGS and SIS. A phenomenological fit, scaling logarithmically with $\sqrt{s_{NN}}$, describes both $dE_T/d\eta$ and $dN_{ch}/d\eta$ well for all energies and for the most central collisions.

Using the fit results, one can separate two regions with different particle production mechanisms. The region below SPS energy is characterized by a steep increase in $E_T/N_{ch} \sim \langle m_T \rangle$ with $\sqrt{s_{NN}}$, whereas for the energies above SPS E_T/N_{ch} is found to be weakly dependent on $\sqrt{s_{NN}}$.

Within the systematic errors of the measurements the shape of the centrality curves of $dN_{ch}/d\eta/(0.5N_p)$ vs. N_p were found to be the same in the range of RHIC energies and to scale with $\ln(\sqrt{s_{NN}})$. The same trend must be true for E_T because E_T/N_{ch} has a very weak centrality dependence.

Based on the $dE_T/d\eta$ measurements, the Bjorken energy density estimates were performed and $\epsilon_{Bj} \cdot \tau$ was determined to be 5.4 ± 0.6 GeV/($fm^2 \cdot c$) at $\sqrt{s_{NN}} = 200$ GeV for the most central bin. This is in excess of what is believed to be sufficient for a phase transition to the new state of matter. The energy density increases by about a factor of 2.6 from SPS to RHIC energy.

Finally, a comparison between the RHIC $dN_{ch}/d\eta$ and $dE_T/d\eta$ data and a collection of models was performed. A few models, notably *HIJING* and *AMPT*, reproduce both $dE_T/d\eta$ and $dN_{ch}/d\eta$ rather well for several energies.

References

- [1] PHENIX Collaboration S.S. Adler *et al.*, nucl-ex/0409015
- [2] H. Hahn *et al.*, Nucl. Instrum. Methods **A499**, 245-263 (2003).
- [3] PHENIX Collaboration, K. Adcox *et al.*, Nucl. Instrum. Methods **A499**, 469-479 (2003).
- [4] K. Adcox *et al.*, Nucl. Instrum. Methods **A497**, 263-293 (2003).
- [5] L. Aphechetché *et al.*, Nucl. Instrum. Methods **A499**, 521-536 (2003).
- [6] M. Allen *et al.*, Nucl. Instrum. Methods **A499**, 549-559 (2003).
- [7] S. Adler *et al.*, Nucl. Instrum. Methods **A470**, 488-499 (2001).
- [8] PHENIX Collaboration, K. Adcox *et al.*, Phys. Rev. Lett. **87**, 052301 (2001).
- [9] PHENIX Collaboration, K. Adcox *et al.*, Phys. Rev. Lett. **86**, 3500 (2001).
- [10] A. Milov for the PHENIX Collaboration, Nucl. Phys. **A698**, 171 (2002).
- [11] A. Bazilevsky for the PHENIX Collaboration, Nucl. Phys. **A715**, 486 (2003).
- [12] D. Silvermyr, Ph.D. Thesis. Lund University (2001).
- [13] A. Milov, Ph.D. Thesis. The Weizmann Institute of Science (2002).
- [14] PHENIX Collaboration, K. Adcox *et al.*, Phys. Rev. Lett. **88**, 242301 (2002).
- [15] GEANT 3.2.1, CERN program library.
- [16] X.N. Wang and M. Gyulassy, Phys. Rev. **D44**, 3501 (1991).
- [17] PHENIX Collaboration, S.S. Adler *et al.*, Phys. Rev. **C69**, 034909 (2004).
- [18] J. Bächler for the NA49 collaboration, Nucl. Phys. **A661**, 45 (1999).
- [19] M. van Leeuwen for the NA49 collaboration, Nucl. Phys. **A715**, 161 (2003).
- [20] NA49 Collaboration, S.V. Afanasiev *et al.*, Phys. Rev. **C66**, 054902 (2002).
- [21] K. Hagiwara *et al.*, <http://pdg.lbl.gov>, Phys. Rev. **D66**, 010001 (2002).
- [22] B. Hahn, D.G. Ravenhall and R. Hofstadter, Phys. Rev. **101**, 1131 (1956), and C.W. De Jager *et al.*, Atomic Data and Nuclear Table **24**, 479 (1974).
- [23] PHOBOS Collaboration, B.B. Back *et al.*, nucl-ex/0210015.
- [24] E-802 Collaboration, T. Abbott *et al.*, Phys. Rev. **C63**, 064602 (2001).
- [25] PHENIX Collaboration, K. Adcox *et al.*, Phys. Rev. **C66**, 024901 (2002).
- [26] WA98 Collaboration, M.M. Aggarwal *et al.*, Eur. Phys. J. **C18**, 651 (2001).
- [27] PHENIX Collaboration, S.S. Adler *et al.*, Phys. Rev. Lett. **91**, 241803-1 (2003).
- [28] M. Gyulassy, nucl-th/0106072.
- [29] A. Krasnitz, Y. Nara, R. Venugopalan, hep-ph/0305112, Nucl. Phys. **A727**, 427-436 (2003).
- [30] J.D. Bjorken, Phys. Rev. **D27**, 140 (1983).
- [31] NA49 Collaboration, T. Alber *et al.*, Phys. Rev. Lett. **75**, 3814 (1995).
- [32] A. Andronic and P. Braun-Munzinger, hep-ph/04022091
- [33] J. Cleymans and K. Redlich, Phys. Rev. Lett. **81**, 5284 (1988).
- [34] P. Braun-Munzinger, K. Redlich and J. Stachel nucl-th/0304013
- [35] M. Gazdzicki for the NA49 Collaboration nucl-ex/0403023
- [36] CERES Collaboration D. Adamova *et al.*, Phys. Rev. Lett. **90**, 022301 (2003).
- [37] A. Appelshäuser for the CERES Collaboration, Nucl. Phys. **A698**, 253c-260c (2002).

- [38] STAR Collaboration, J. Adams *et al.*, nucl-ex/0311017.
- [39] BRAHMS Collaboration, I.G. Bearden *et al.*, Phys. Lett. **B523**, 227 (2001).
- [40] BRAHMS Collaboration, I.G. Bearden *et al.*, Phys. Rev. Lett. **88**, 202301 (2002).
- [41] PHOBOS Collaboration, B.B. Back *et al.*, Phys. Rev. Lett. **85**, 3100 (2000).
- [42] PHOBOS Collaboration, B.B. Back *et al.*, Phys. Rev. **C65**, 061901 (2002).
- [43] M.D. Baker *et al.* for the PHOBOS Collaboration,, Nucl. Phys. **A715**, 65c-74c (2003).
- [44] T.S. Ullrich for the STAR Collaboration, nucl-ex/0305018.
- [45] T.S. Ullrich for the STAR Collaboration, Nucl. Phys. **A715**, 399 (2003).
- [46] STAR Collaboration, J. Adams *et al.*, nucl-ex/0407003.
- [47] D. Miškowicz for the CERES Collaboration, Proc. of CIPPQG Palaiseau, September 2001.
- [48] NA50 Collaboration, M.C. Abreu *et al.*, Phys. Lett. **B530**, 43 (2002).
- [49] NA57 Collaboration, F. Antinori *et al.*, nucl-ex/0406004.
- [50] PHOBOS Collaboration, B.B. Back *et al.*, nucl-ex/0301017
- [51] UA5 Collaboration, G.J. Alner *et al.*, Z. Phys. **C33**, 1-6 (1986).
- [52] W. Thome *et al.*, Nucl. Phys. **B129**, 365-389 (1977).
- [53] J. Whitmore, Phys. Repts. **10**, 274-373 (1974).
- [54] V. Blobel *et al.*, Nucl. Phys. **B69**, 454-492 (1974).
- [55] V. Topor Pop, M. Gyulassy, J. Barrette, C. Gale, X. N. Wang, N. Xu, and K. Filimonov, Phys. Rev. **C68**, 054902 (2003).
- [56] B. Andersson *et al.*, Nucl. Phys. **B281**, 289 (2003).
- [57] K.J. Eskola *et al.*, Nucl. Phys. **B570**, 379 (2000); Phys. Lett. **B497**, 39 (2001).
- [58] D. Kharzeev and M. Nardi, Phys. Lett. **B507**, 121 (2001); D. Kharzeev and E. Levin, Phys. Lett. **B523**, 79 (2001).
- [59] S. Lee and X.N. Wang, Phys. Lett. **B527**, 85 (2002).
- [60] Y.Nara, Nucl. Phys. **A638**, 555c (1998).
- [61] Z. Lin *et al.*, Phys. Rev. **C64**, 011902 (2001).
- [62] A. Accardi, Phys. Rev. **C64**, 064905 (2001).
- [63] R. Ugoccioni, Phys. Lett. **B491**, 253 (2000).
- [64] A. Capella *et al.*, Phys. Repts. **236**, 225 (1994).
- [65] N. Armesto Perez *et al.*, Phys. Lett. **B527**, 92 (2002); Eur. Phys. J. **C22**, 149 (2001).
- [66] D.E. Kahana and S.H. Kahana, nucl-th/0208063.
- [67] S. Jeon and J. Kapusta, Phys. Rev. **C63**, 011901 (2001).
- [68] F. Ceretto, Ph.D. Thesis. University of Heidelberg (1998).
- [69] H. Appelshäuser for the CERES Collaboration, Nucl. Phys. **A698**, 253 (2002).
- [70] E802 Collaboration, L. Ahle *et al.*, Phys. Rev. **C59**, 2173 (1999).
- [71] E802 Collaboration, L. Ahle *et al.*, Phys. Rev. **C58**, 3523-3538 (1998).
- [72] C.A. Ogilvie for the E866 and E917 Collaborations, Nucl. Phys. **A638**, 57c-68c (1998).
- [73] Y. Akiba for the E802 Collaboration, Nucl. Phys. **A610**, 139 (1996).
- [74] E917 Collaboration, B.B. Back *et al.*, Phys. Rev. Lett. **86**, 1970-1973 (2001).
- [75] E802 Collaboration, L. Ahle *et al.*, Phys. Rev. **C57**, R466-R470 (1998).
- [76] E802 Collaboration, L. Ahle *et al.*, Phys. Lett. **B476**, 1 (2000).
- [77] E802 Collaboration, L. Ahle *et al.*, Phys. Lett. **B490**, 53 (2000).
- [78] FOPI Collaboration, W. Reisdorf *et al.*, Nucl. Phys. **A612**, 493 (1997).
- [79] FOPI Collaboration, D. Pelte *et al.*, Z. Phys. **A357**, 215 (1997).
- [80] FOPI Collaboration, B. Hong *et al.*, Phys. Rev. **C66**, 034901 (2002).